Control of Spatial Correlations between Rydberg Excitations using Rotary Echo

N. Thaicharoen, A. Schwarzkopf, and G. Raithel

Phys. Rev. Lett. **118**, 133401 — Published 31 March 2017

DOI: 10.1103/PhysRevLett.118.133401

Control of spatial correlations between Rydberg excitations using rotary echo

N. Thaicharoen*, A. Schwarzkopf†, and G. Raithel
Department of Physics, University of Michigan, Ann Arbor, Michigan 48109, USA
(Dated: February 21, 2017)

We manipulate correlations between Rydberg excitations in cold atom samples using a rotary-echo technique in which the phase of the excitation pulse is flipped at a selected time during the pulse. The correlations are due to interactions between the Rydberg atoms. We measure the resulting change in the spatial pair correlation function of the excitations via direct position-sensitive atom imaging. For zero detuning of the lasers from the interaction-free Rydberg-excitation resonance, the pair-correlation value at the most likely nearest-neighbor Rydberg-atom distance is substantially enhanced when the phase is flipped at the middle of the excitation pulse. In this case, the rotary echo eliminates most uncorrelated (un-paired) atoms, leaving an abundance of correlated atom pairs at the end of the sequence. In off-resonant cases, a complementary behavior is observed. We further characterize the effect of the rotary-echo excitation sequence on the excitation-number statistics.

PACS numbers: 32.80.Ee, 34.20.Cf, 32.80.Qk

Recently there has been a growing interest in applications of correlated Rydberg-atom systems. The correlations arise from strong electrostatic interactions between Rydberg atoms, leading to an excitation blockade [1–3]. The correlations have been utilized to realize non-classical light sources, such as single-photon and correlated-photon sources [4]. Blockaded Rydberg-atom samples can exhibit sub-Poissonian statistics for the Rydberg-atom number distribution [5–7]. Higher-order correlation leads to Rydberg-atom aggregation [7–11] and crystallization of Rydberg excitations [12–14].

In previous studies, the correlations between Rydberg atoms have been enhanced by detuning the excitation laser to match the van der Waals energy level shift at a well-defined pair separation [15, 16]. Another method to control Rydberg-atom correlations, proposed by Wüster *et. al.* [17], is based on a rotary excitation echo. As found previously, in simulations [18] and in experiments [19, 20], the echo occurs when the sign of the Rabi frequency is flipped in the middle of the excitation pulse. The rotary-echo technique can also be used in Rydberg-atom interferometry [21, 22]. It was predicted in [17] that a rotary-echo excitation pulse leads to an enhancement of the Rydberg pair correlation function at a separation near the blockade radius.

In the present work, we employ a rotary-echo sequence to excite cold ^{85}Rb atoms into Rydberg states. We use a position-sensitive Rydberg-atom imaging and counting method [15] to explore the effects of the echo on spatial Rydberg-atom correlations and the excitation-number statistics. Both these observables for correlation in cold Rydberg-atom ensembles have been studied previously in the absence of a rotary echo (see [15, 23] and [5–7], respectively). We demonstrate that a rotary-echo sequence can enhance spatial correlations between the Rydberg excitations. We further observe that the rotary echo strongly affects the counting number statistics of Rydberg excitations. We establish that the rotary-echo-induced features strongly depend on the laser detuning. Particularly, it is seen that the rotary echo gives rise to strong correlations when the excitation lasers are on-resonant, while in off-resonant cases the echo causes the destruction of spatial correlations that would otherwise be present.

Schematics of the experiment and the timing sequence are presented in Fig. 1. Cold ^{85}Rb atoms in the $5S_{1/2}$

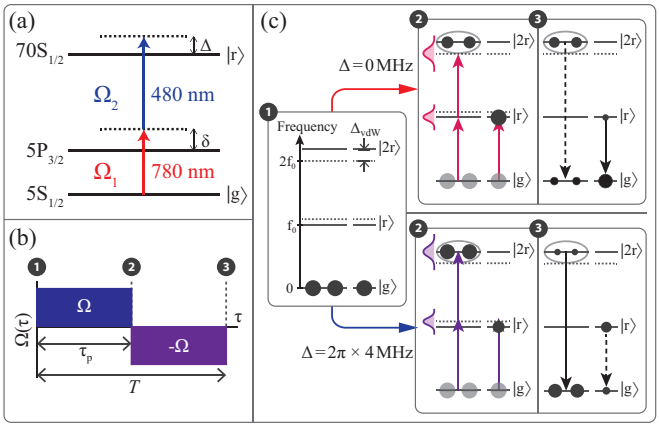

FIG. 1. (a) Two-photon excitation of a single ^{85}Rb Rydberg atom. (b) Echo sequence during excitation. We apply an excitation pulse of duration $T = 250$ ns. The two-photon Rabi frequency is switched from Ω to $-\Omega$ (in the field picture) at time τ_p. The time labels 1, 2, and 3 above the timing sequence correspond with (c). (c) Dynamics of atoms during the echo sequence. The frequency to excite one Rydberg atom $|r\rangle$ without interactions is f_0 (red arrow). The frequency leading to direct excitation of two Rydberg atoms (state $|2r\rangle$) is $f_0 + \Delta_{vdW}/2$ (purple arrow). Because of the excitation bandwidth, in either case we excite a mix of isolated Rydberg atoms in state $|r\rangle$ and Rydberg-atom pairs in state $|2r\rangle$. The circle sizes in the level diagrams illustrate the populations of van-der-Waals-interacting atom pairs (left pair of circles) and of isolated atoms (right circle) at times 1, 2 and 3 for the cases $\Delta = 0$ and $\Delta = 2\pi \times 4$ MHz.

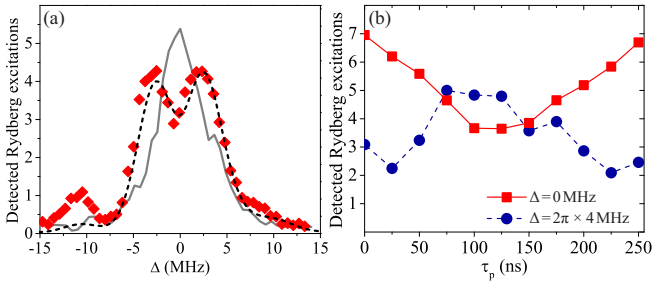

FIG. 2. (a) Experimental Rydberg excitation spectra for $\tau_p = 0$ (gray solid line) and 125 ns (red diamonds) and simulated spectrum scaled to match the experiment for $\tau_p = 125$ ns (black dashed line). (b) Number of detected Rydberg excitations as a function of phase flip time τ_p for $\Delta = 0$ and $2\pi \times 4$ MHz.

state are excited to the $70S_{1/2}$ state via two-photon excitation by simultaneously applying 780- and 480-nm laser pulses with a duration $T = 250$ ns. The 780-nm laser has a Gaussian beam parameter $w_0 = 0.75$ mm and a power of 600 μW. The 480-nm laser has a $w_0 \approx 8$ μm and a power of 30 mW. The detuning from the intermediate state $5P_{3/2}$ is $\delta = 2\pi \times 131$ MHz. At the beam center, the Rabi frequencies of the lower and upper transitions are $\Omega_1 = 2\pi \times 20$ MHz and $\Omega_2 = 2\pi \times 22$ MHz, respectively, leading to a two-photon (one 780 nm and one 480 nm photon) Rabi frequency for single-atom excitation at the two-photon resonance ($\Delta = 0$) of $\Omega = \Omega_1\Omega_2/(2\delta) = 2\pi \times 1.71$ MHz. In the case of substantial detuning $\Delta > 0$, Rydberg atoms may instead be directly excited in pairs at a separation where the detuning Δ matches the van der Waals interaction Δ_{vdW}. When $\Delta = 2\pi \times 4$ MHz, the Rabi frequency for the simultaneous excitation of such pairs is $\Omega_{pair} = \Omega^2/(2\Delta) = 2\pi \times 0.37$ MHz.

At $\Delta = 2\pi \times 4$ MHz, atom pairs are efficiently excited at a measured pair separation $R \approx 10$ μm, where the excess energy associated with the laser excitation of the atoms equals the van-der-Waals shift, $\Delta \approx \Delta_{vdW} = C_6/R^6$, where C_6 is the van-der-Waals dispersion coefficient [15, 16]. This effect arises because the presence of Rydberg atoms in the sample facilitates the addition of new Rydberg atoms at a fairly well-defined radius that depends on laser detuning and interaction strength [7–11]. The atom pairs at the most likely distance ($R \approx 10$ μm) can be excited both via sequential (facilitated) as well as direct (two-photon) excitation.

To implement a rotary echo, we shift the phase of the radio frequency (RF) signal applied to the acousto-optic modulator that determines the optical phase of the 480-nm pulse. We use a 180°-power splitter together with a high-isolation RF switch to change the phase of the RF signal by π at time τ_p after the excitation lasers are turned on [see Fig. 1(b)]. The phase-flip time τ_p is varied from 0 to 250 ns, with a step size of 25 ns. Immediately after the excitation pulse, we field-ionize the Rydberg atoms by applying a high voltage to a tip imaging probe (TIP). The field ions are counted and their positions measured using a position-sensitive microchannel plate and phosphor screen assembly (MCP) with a CCD camera. Each CCD image contains blips whose positions represent the 2-dimensional projection of the positions of the parent Rydberg atoms in the excitation region. The excitation region is determined by the 480-nm beam position, which is centered 470 μm above the TIP, providing a magnification of 150 (see Ref. [16] for the magnification calibration). For each detuning Δ and flip time τ_p we take 10000 images and choose the 5000 images with the highest numbers of excitations to calculate pair correlation images. Angular integrals of the pair correlation images yield the radial pair correlation functions $I(R)$. Quantitative information on the echo effect is then extracted from the $I(R)$.

To verify the rotary echo [18–20] in our experiment, we measure Rydberg excitation spectra for $\tau_p = 0$ and 125 ns, as shown in Fig. 2(a). The peak position in the echo-free spectrum ($\tau_p = 0$) marks the on-resonant transition $\Delta = 0$. The echo occurs when $\tau_p \approx T/2$. In this case, the spectra are broader and have a depression of detected Rydberg counts at $\Delta = 0$ [Fig. 2(a)]; the $\Delta = 0$ counts have a minimum when $\tau_p = T/2 = 125$ ns [Fig. 2(b)], as expected for a rotary echo.

In Fig. 2(a), the signal does not drop to zero at $\Delta = 0$, as would be the case for a perfect echo because slightly off-resonantly excited atom pairs whose pair energies are shifted due to the van der Waals interactions do not undergo a perfect echo. This is the effect we essentially exploit later in this work. Further, the spectrum is convolved with the profile of the shot-to-shot laser-frequency jitter. We have simulated the excitation spectra of atom pairs in a disordered atomic sample and convolved the results with a Gaussian profile for the frequency jitter. Assuming a full-width-at-half-maximum (FWHM) of 3 to 4 MHz for the Gaussian profile and using the measured pulse shape, we obtain simulated spectra that are consistent with the experimental ones [see Fig. 2(a)]. The simulated spectrum is a weighted average over the nearest-neighbor distribution in a randomly distributed ground state atom sample. Interactions between more than two atoms are neglected.

We now turn to describing the effect of the echo sequence on the spatial pair-correlation functions and the Rydberg-atom-counting statistics. Pair correlation images measured for $\Delta = 0$ MHz are shown in the top row of Fig. 3(a). When τ_p is increased from 0 or decreased from T towards $T/2$, the pair correlation image develops an enhancement ring with a radius of about 10 μm. Inspection of the images in the top row of Fig. 3(a) shows that the enhancement ring reaches maximal contrast for $\tau_p \approx T/2 = 125$ ns. For the case $\Delta = 2\pi \times 4$ MHz [bottom row of Fig. 3(a)], the pair correlation is maximally enhanced at a radius near 10 μm when $\tau_p \approx 0$ or T, while

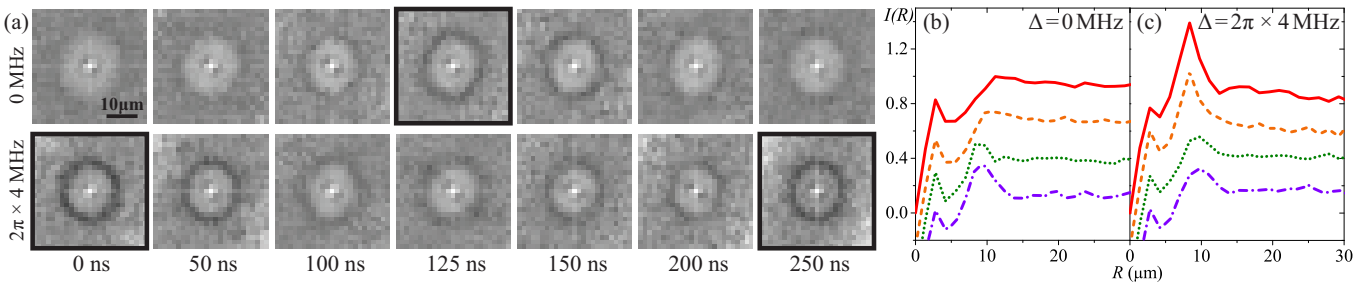

FIG. 3. (a) Pair correlation images at selected τ_p for (top row) $\Delta = 0$ MHz and (bottom row) $\Delta = 2\pi \times 4$ MHz. The linear grayscale ranges from 0 (white) to 2 (black) where values of 1, <1, and >1 indicate no correlation, anticorrelation, and positive correlation, respectively. The bold borders indicate pair correlation images obtained from systems that contain many pair-excitations. The 3 to 4 μm pattern near the center of each image is an artifact (see text). (b) Angular integrals $I(R)$ of the pair correlation images for $\Delta = 0$ MHz for $\tau_p = 0$, 50, 100, and 125 ns (top to bottom). The vertical axis is for the 0 ns curve. The other curves are shifted down in equidistant intervals of 0.3 for clarity. (c) Same as (b), but for $\Delta = 2\pi \times 4$ MHz.

it becomes washed out when $\tau_p \approx T/2$. We note that the clarity of the enhancement ring is reduced because we measure the 2-dimensional projection of a 3-dimensional distribution. We have verified that the projection does not significantly affect the diameter of the enhancement ring. Further, the pair-correlation signal at very short distances (about 3 μm) is an artifact caused by ion feedback from the TIP; field electrons impacting on the TIP release a secondary ion that impacts the MCP close to the primary (Rb^+) ion [24]. In our quantitative analysis below, we employ the angular integrals $I(R)$ of the pair correlation images. We show the $I(R)$ curves in Fig. 3(b) for the case $\Delta = 0$, and in Fig. 3(c) for the case $\Delta = 2\pi \times 4$ MHz.

In the explanation of the pair correlation data and the strength of the correlation enhancement, we concentrate on the "echo case" $\tau_p \approx T/2$ and refer to Fig. 1. The two-photon Rabi frequency ($\Omega = 2\pi \times 1.71$ MHz) is high enough that many excitation domains within the sample carry one Rydberg excitation (state $|r\rangle$) after the first phase of the excitation pulse [*i.e.*, at time τ_p; isolated atom in Fig. 1(c)]. However, due to the bandwidth of the excitation pulse, some excitation domains become populated with a Rydberg-excitation pair (state $|2r\rangle$). The doubly-excited domains have an energy shift Δ_{vdW} from the drive field due to the van der Waals interaction [atom pairs in Fig. 1(c)]. The atom populations after flipping the phase and completing the excitation pulse are illustrated in Fig. 1(c), at time labels 3. For the case $\Delta = 0$, domains in the state $|r\rangle$ are de-excited back to the $|g\rangle$-state. However, the domains in excited state $|2r\rangle$ are off-resonant, leaving them with some probability in $|2r\rangle$ after completion of the echo sequence. In essence, after the sequence we expect to find a relative over-abundance of atoms separated by a distance near the blockade radius. The experimental data support this scenario. A complementary behavior occurs in the case $\Delta = 2\pi \times 4$ MHz, with the roles of singly- and doubly-excited domains reversed.

For a quantitative analysis, from the $I(R)$ curves we obtain peak values I_{max} and radii R_{max} of maximal correlation enhancement, determined by local parabolic fits to the maxima near $R = 10$ μm. We calculate S, the strength of the pair correlation enhancement, as:

$$S = (I_{max} - \langle I \rangle)/\langle I \rangle \quad . \tag{1}$$

We determine the asymptotic values $\langle I \rangle$ by taking the average of $I(R)$ over the range 20 μm $< R <$ 60 μm. Figure 4 shows the dependence of S and R_{max} on τ_p; panels (a) and (b) are for $\Delta = 0$ and $2\pi \times 4$ MHz, respectively. As anticipated from Fig. 3, we see in Fig. 4(a) and Fig. 4(b) that the curves $S(\tau_p)$ exhibit pronounced maxima at the "echo case" $\tau_p \approx T/2$, when $\Delta = 0$, and at the "no-echo case" $\tau_p \approx 0$ and T, when $\Delta = 2\pi \times 4$ MHz. Thus, the curves $S(\tau_p)$ for $\Delta = 0$ and $2\pi \times 4$ MHz exhibit complementary trends.

Close inspection of the $I(R)$ curves in Figs. 3(b-c) shows that the FWHM of the enhancement peak decreases when the I_{max} increases. Further, Figs. 4(a) and (b) reveal a dependence of R_{max} on τ_p. In particular, it is seen in Figs. 3(b) and 4(a) that R_{max} for $\tau_p = T/2$ drops to near or slightly below the blockade radius seen for $\tau_p \approx 0$. To qualitatively understand this, we note that for $\tau_p \approx T/2$ the Fourier width of the excitation pulse at the time instant of the phase flip is twice as large as the Fourier width for $\tau_p \approx 0$ at the end of the entire excitation pulse. Hence, the blockade radius relevant in the case $\tau_p \approx T/2$ is smaller than that in the case $\tau_p \approx 0$. It is therefore plausible for $R_{max}(T/2)$ to drop near or slightly below the blockade radius seen at $\tau_p \approx 0$.

Figure 4 demonstrates that, both for $\Delta = 0$ and $2\pi \times 4$ MHz, the values for R_{max} are smaller for larger values of S. The relationship between R_{max} and S is shown in Fig. 4(c). The value S increases from near zero to ~ 0.8 as the radius of maximal correlation diminishes from $\sim$ 13 μm to $\sim$ 8 μm. Also, the $S(R_{max})$ dependencies extracted from the $\Delta = 0$ and $2\pi \times 4$ MHz measurements agree well within their overlap region, 9 μm

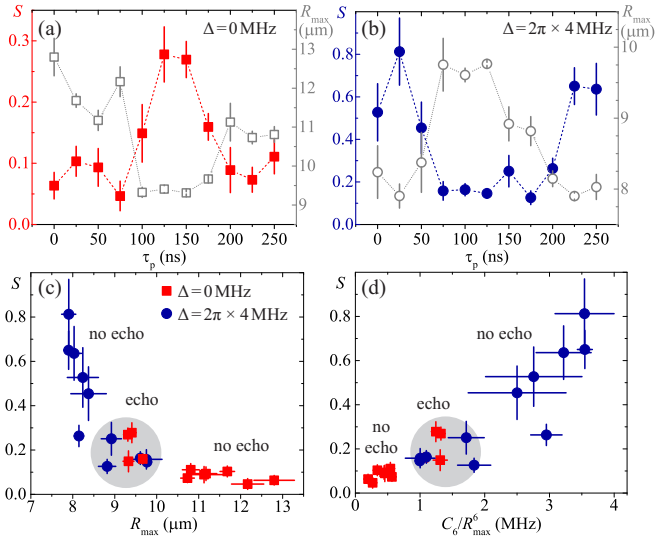

FIG. 4. Pair correlation enhancement, S (■ and ●) and $R_{\max}$ (□ and ○) as a function of τ_p for (a) $\Delta = 0$ MHz and (b) $\Delta = 2\pi \times 4$ MHz, respectively. (c) S versus $R_{\max}$. (d) S versus $C_6/R^6_{\max}$. In the plots (c) and (d), we identify the cases of excitation with and without echo for both $\Delta = 0$ and 4 MHz.

$< R_{\max} < 10$ μm. The rotary-echo sequence therefore provides an ability to control the most probable separation between atom pairs. It is noted that the value of S changes substantially over the range of accessible separation distances. Fig. 4(d) shows that S is qualitatively proportional to the van der Waals interaction strength C_6/R^6 at $R_{\max}$. While this may seem reasonable, an explanation of this behavior will require more investigation.

We have established that the echo excitation sequence has a profound effect on spatial correlations in cold Rydberg-atom samples. We expect a related effect in the Rydberg excitation counting statistics, which should also carry signatures of the correlations in the system. A measure to characterize counting-statistics is the Mandel Q-value [5–7, 25],

$$Q = \frac{\langle n(\tau_p)^2 \rangle - \langle n(\tau_p) \rangle^2}{\langle n(\tau_p) \rangle} - 1 \quad . \tag{2}$$

Figure 5 shows the Q-values versus τ_p. The plotted values do not take the detection efficiency η into account; the actual Q-values in the sample are given by Q/η. The Q-values observed for $\Delta = 0$ MHz [Fig. 5(a)] are mostly negative, ranging from -0.10 to 0.02, while the ones for $\Delta = 2\pi \times 4$ MHz [Fig. 5(b)] are positive, ranging from 0.03 to 0.25. This shows that for $\Delta = 0$ and $\tau_p \sim 0$ and $\sim T$ the atoms largely follow sub-Poissonian statistics ($Q < 0$), while for $\Delta = 2\pi \times 4$ MHz and $\tau_p = 0$ and T they follow super-Poissonian statistics ($Q > 0$).

In the following we explain the trends observed in our Q-value measurements. For the case of on-resonant excitation without echo, the atom counting statistics is sub-

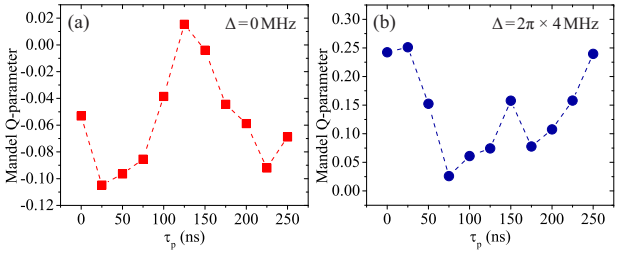

FIG. 5. Q-value as a function of τ_p for (a) $\Delta = 0$ MHz and (b) $\Delta = 2\pi \times 4$ MHz.

Poissonian (Q<0) due to a blockade effect [5], as demonstrated in Fig. 5(a) at τ_p near 0 and 250 ns. In contrast, the Q-values for systems containing mostly pair-excitations are expected to trend toward positive values [17, 26], indicating super-Poissonian distributions. This effect is demonstrated in Fig. 5, in which the Q-values reach high values when pair excitations are dominant. This is the case for $\tau_p = 125$ ns at $\Delta = 0$ MHz [Fig. 5(a)], and $\tau_p = 0$ and 250 ns at $\Delta = 2\pi \times 4$ MHz [Fig. 5(b)]. These cases correspond to the images with bold borders in Fig. 3(a).

For a qualitative explanation of why ensembles of correlated Rydberg-atom pairs lead to super-Poissonian statistics, we consider a Poissonian distribution of atom pairs ($Q_{\text{pair}} = 0$). Since every pair contains two atoms, we substitute $n = 2n_{\text{pair}}$ into Eq. 2. The relation between Q_{pair} and the Q-value for single-atom detections, Q_{single}, is seen to be

$$Q = Q_{\text{single}} = 2Q_{\text{pair}} + 1 \quad . \tag{3}$$

Hence, a Poissonian distribution of uncorrelated Rydberg-atom pairs ($Q_{\text{pair}} = 0$) results in a super-Poissonian distribution of single-atom detections ($Q_{\text{single}} = 1$). Considering that the detection efficiency is $\eta \sim 0.3$, we expect a measured $Q \sim 0.3$, which is close to the value shown in Fig. 5(b) at $\tau_p = 0$ and T.

In summary we have measured the effect of the rotary echo on spatial pair correlation functions and counting statistics of Rydberg atoms for on- and off-resonant excitations. The measurements exhibit the connection between spatial correlations and counting statistics. The result also shows that it is possible to prepare correlated Rydberg atoms at a well-defined interatomic separation by using this method. This ability could be useful in atom kinetics experiments [16, 24]. To make the method attractive for such applications, it is desirable to find conditions in which the pair correlation enhancement obtained with the echo method exceeds that obtained with plain off-resonant excitation (see Fig. 4). This may be achievable, in the future, by reducing the excitation bandwidth and possibly by shaping amplitude and phase of the excitation pulse. Further, it would be interesting to explore the effect of the echo sequence in the case of

anisotropic interaction potentials.

This work was supported by the NSF (PHY-1506093) and the AFOSR (FA9550-10-1-0453). N.T. acknowledges support from DPST of Thailand. We thank S. Wüster for helpful discussions.

*nithi@umich.edu
†Present address: zeroK NanoTech Corporation, Gaithersburg, MD 20879, USA

[1] M. D. Lukin, M. Fleischhauer, R. Cote, L. M. Duan, D. Jaksch, J. I. Cirac, and P. Zoller, Phys. Rev. Lett. **87**, 037901 (2001).
[2] E. Urban, T. A. Johnson, T. Henage, L. Isenhower, D. D. Yavuz, T. G. Walker, and M. Saffman, Nat Phys **5**, 110 (2009).
[3] T. M. Weber, M. Höning, T. Niederprüm, T. Manthey, O. Thomas, V. Guarrera, M. Fleischhauer, G. Barontini, and H. Ott, Nat Phys **11**, 157 (2015).
[4] Y. O. Dudin and A. Kuzmich, Science **336**, 887 (2012).
[5] T. C. Liebisch, A. Reinhard, P. R. Berman, and G. Raithel, Phys. Rev. Lett. **95**, 253002 (2005).
[6] N. Malossi, M. Valado, S. Scotto, P. Huillery, P. Pillet, D. Ciampini, E. Arimondo, and O. Morsch, Phys. Rev. Lett. **113**, 023006 (2014).
[7] H. Schempp, G. Günter, M. Robert-de Saint-Vincent, C. S. Hofmann, D. Breyel, A. Komnik, D. W. Schönleber, M. Gärttner, J. Evers, S. Whitlock, and M. Weidemüller, Phys. Rev. Lett. **112**, 013002 (2014).
[8] T. Amthor, C. Giese, C. S. Hofmann, and M. Weidemüller, Phys. Rev. Lett. **104**, 013001 (2010).
[9] M. Gärttner, K. P. Heeg, T. Gasenzer, and J. Evers, Phys. Rev. A **88**, 043410 (2013).
[10] I. Lesanovsky and J. P. Garrahan, Phys. Rev. A **90**, 011603 (2014).
[11] A. Urvoy, F. Ripka, I. Lesanovsky, D. Booth, J. Shaffer, T. Pfau, and R. Löw, Phys. Rev. Lett. **114**, 203002 (2015).
[12] T. Pohl, E. Demler, and M. D. Lukin, Phys. Rev. Lett. **104**, 043002 (2010).
[13] P. Schauß, M. Cheneau, M. Endres, T. Fukuhara, S. Hild, A. Omran, T. Pohl, C. Gross, S. Kuhr, and I. Bloch, Nature **491**, 87 (2012).
[14] P. Schauß, J. Zeiher, T. Fukuhara, S. Hild, M. Cheneau, T. Macrì, T. Pohl, I. Bloch, and C. Gross, Science **347**, 1455 (2015).
[15] A. Schwarzkopf, D. A. Anderson, N. Thaicharoen, and G. Raithel, Phys. Rev. A **88**, 061406 (2013).
[16] N. Thaicharoen, A. Schwarzkopf, and G. Raithel, Phys. Rev. A **92**, 040701 (2015).
[17] S. Wüster, J. Stanojevic, C. Ates, T. Pohl, P. Deuar, J. F. Corney, and J. M. Rost, Phys. Rev. A **81**, 023406 (2010).
[18] J. V. Hernández and F. Robicheaux, J. Phys. B: At. Mol. Opt. Phys. **41**, 195301 (2008).
[19] U. Raitzsch, V. Bendkowsky, R. Heidemann, B. Butscher, R. Löw, and T. Pfau, Phys. Rev. Lett. **100**, 013002 (2008).
[20] K. C. Younge and G. Raithel, New J. Phys. **11**, 043006 (2009).
[21] A. Dunning, R. Gregory, J. Bateman, N. Cooper, M. Himsworth, J. A. Jones, and T. Freegarde, Phys. Rev. A **90**, 033608 (2014).
[22] L. Wang, H. Zhang, L. Zhang, G. Raithel, J. Zhao, and S. Jia, Phys. Rev. A **92**, 033619 (2015).
[23] A. Schwarzkopf, R. E. Sapiro, and G. Raithel, Phys. Rev. Lett. **107**, 103001 (2011).
[24] N. Thaicharoen, L. Gonçalves, and G. Raithel, Phys. Rev. Lett. **116**, 213002 (2016).
[25] C. Ates, T. Pohl, T. Pattard, and J. M. Rost, J. Phys. B: At. Mol. Opt. Phys. **39**, L233 (2006).
[26] K. P. Heeg, M. Gärttner, and J. Evers, Phys. Rev. A **86**, 063421 (2012).